



**HAL**  
open science

## Efficient start-to-end 3D envelope modeling for two-stage laser wakefield acceleration experiments

Francesco Massimo, Arnaud Beck, Julien Dérouillat, Mickael Grech, Mathieu Lobet, Frédéric Pérez, Imen Zemzemi, Arnd Specka

► **To cite this version:**

Francesco Massimo, Arnaud Beck, Julien Dérouillat, Mickael Grech, Mathieu Lobet, et al.. Efficient start-to-end 3D envelope modeling for two-stage laser wakefield acceleration experiments. *Plasma Physics and Controlled Fusion*, 2019, 61 (12), pp.124001. 10.1088/1361-6587/ab49cf. hal-02393454

**HAL Id: hal-02393454**

**<https://hal.science/hal-02393454v1>**

Submitted on 10 Dec 2019

**HAL** is a multi-disciplinary open access archive for the deposit and dissemination of scientific research documents, whether they are published or not. The documents may come from teaching and research institutions in France or abroad, or from public or private research centers.

L'archive ouverte pluridisciplinaire **HAL**, est destinée au dépôt et à la diffusion de documents scientifiques de niveau recherche, publiés ou non, émanant des établissements d'enseignement et de recherche français ou étrangers, des laboratoires publics ou privés.

# Efficient start-to-end 3D envelope modeling for two-stage laser wakefield acceleration experiments

F. Massimo<sup>1</sup>, A. Beck<sup>1</sup>, J. Derouillat<sup>2</sup>, M. Grech<sup>3</sup>, M. Lobet<sup>2</sup>, F. Pérez<sup>3</sup>, I. Zemzemi<sup>1</sup> and A. Specka<sup>1</sup>

<sup>1</sup> Laboratoire Leprince-Ringuet – École polytechnique, CNRS-IN2P3, Palaiseau 91128, France

<sup>2</sup> Maison de la Simulation, CEA, CNRS, Université Paris-Sud, UVSQ, Université Paris-Saclay, F-91191 Gif-sur-Yvette, France

<sup>3</sup> Laboratoire d'Utilisation des Lasers Intenses, CNRS, École polytechnique, CEA, Université Paris-Saclay, UPMC Université Paris 06: Sorbonne Universités, F-91128 Palaiseau Cedex, France

E-mail: massimo@l1r.in2p3.fr

Plasma Physics and Controlled Fusion

**Abstract.** Three dimensional Particle in Cell simulations of Laser Wakefield Acceleration require a considerable amount of resources but are necessary to have realistic predictions and to design future experiments. The planned experiments for the Apollon laser also include two stages of plasma acceleration, for a total plasma length of the order of tens of millimeters or centimeters. In this context, where traditional 3D numerical simulations would be computationally very expensive, we present the results of the application of a recently proposed envelope method, to describe the laser pulse and its interaction with the plasma without the need to resolve its high frequency oscillations. The implementation of this model in the code SMILEI is described, as well as the results of benchmark simulations against standard laser simulations and applications for the design of two stage Apollon experiments.

## 1. Introduction

The maximum electric field sustainable by an accelerating cavity determines the minimum size of a particle accelerator. The breakdown limits of the metallic accelerating cavities in conventional accelerators motivated the accelerator community to find alternative technologies to achieve higher accelerating gradients and thus smaller particle accelerators. One of the most promising of these technologies to accelerate electrons is the Laser Wakefield Acceleration (LWFA), i.e. their acceleration by plasma waves generated in the wake of an intense laser pulse propagating along an under dense plasma [1–4]. The future realization of the Apollon laser [5], will pave the way to novel LWFA experiments with high laser power.

The importance of modeling in the LWFA field can hardly be overestimated, since it represents a tool of experimental design, physical prediction, analysis and understanding of the involved phenomena. Nonetheless, LWFA modeling implies significant numerical challenges, which require the use of High Performance Computing (HPC) techniques. The state-of-the-art type of codes used to model LWFA is the Particle in Cell (PIC) [6] code, which samples the plasma distribution function through macro-particles (MP), pushed by and generating electromagnetic (EM) fields defined on a mesh. Vlasov's equation is thus solved following its characteristics, i.e. the MP equations of motion. The PIC method self-consistently updates at each iteration the MP positions and momenta and the EM fields they generate, as well as external EM fields such as a laser pulse. In LWFA simulations, the largest scales to consider are defined by the size of the plasma accelerator. For centimeters long accelerating stages, the total propagation time is of the order of hundreds of picoseconds. On the other hand, the smallest scales are usually defined by the laser. Indeed, the standard PIC method imposes to resolve the laser wavelength  $\lambda_0$  and period  $2\pi/\omega_0$  which are respectively of the order of the micron and the femtoseconds. The discrepancy in scales quickly demonstrates that realistic 3D or quasi-3D [7] simulations of this nature are very costly. This kind of simulation would quickly fall beyond the commonly available amount of computing resources when applied to multi-stage LWFA setups, reaching tens of centimeters. In this context, we call standard laser techniques and standard laser simulations those not using physical approximations or changes of reference frame to speed-up the calculations. Examples of these non-standard techniques include, but are not limited to, quasi-static approximation [8, 9], Azimuthal Fourier decomposition [10], boosted frame techniques [11] or hybrid models [12–14].

A possible technique to reduce the computing cost of LWFA simulations consists in using a description of the laser pulse that takes into account only its complex envelope, with length and transverse size of the order of the

plasma wavelength  $\lambda_p \gg \lambda_0$ , without the need to resolve each optical cycle of the laser in time and space [9,13,15–18]. The code WAKE was one of the first codes with a laser envelope model to simulate laser wakefield scenarios [9]. However, the quasi-static approximation (QSA) of the code prevented the simulation of electrons injection. Time explicit (i.e. without QSA) envelope codes were developed, with implicit schemes to solve the evolution equation of the laser envelope [13,15,17,18]. The use of implicit solvers to solve an envelope equation requires non-trivial parallelization techniques to be used in 3D, as they often require the inversion of a matrix representing a transverse differential operator acting on the envelope [13,17–19]. Recently, a time explicit 3D envelope code with an easily parallelizable explicit solver for the envelope equation has been developed in the PIC code ALaDyn [20].

In this paper, we present applications of this technique now also implemented in the PIC code SMILEI [21,22], to demonstrate its suitability for studies oriented to the LWFA experiments planned for Apollon.

In the second section, we briefly review the envelope model’s approximations and equations. In the third section a numerical simulation of a second stage experiment is discussed, comparing its results with a standard laser simulation. In the fourth section, the results of four simulations of possible working points for single stage experiments are reported. In the Appendix, the envelope model equations and their solution in SMILEI are summarized.

## 2. Review of the envelope model

In many typical situations for LWFA, the spatial and temporal scales of interest (e.g. the wavelength of the accelerating plasma wave, scaling as  $\lambda_p$ ) are significantly larger than the scales related to the laser central wavelength  $\lambda_0$ . In these cases, if the laser pulse is much longer than  $\lambda_0$ , the computation time can be substantially reduced if one could sample only the laser envelope characteristic length (which normally scales as  $\lambda_p$  as well in typical LWFA setups) instead of  $\lambda_0$ , as depicted in Fig. 1. With this lower resolution, the region of interest for the electron acceleration, i.e. the end of the plasma “bubble” in the first period of the plasma wave behind the laser, would still be correctly described in most of the situations of interest for LWFA. Indeed, the bubble formation is triggered by an averaged interaction of the particles with the laser, i.e. the ponderomotive force [23], which derives from the laser envelope.

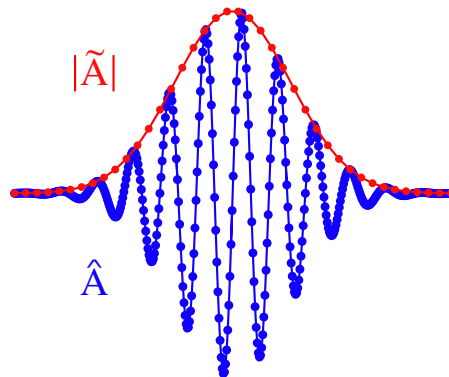


Figure 1: Blue line: laser vector potential component  $\hat{A}$  along the polarization direction. Red line: the module of its complex envelope  $|\tilde{A}|$ . The envelope is sampled by a number of points smaller by a factor ten compared to  $\hat{A}$ . In this example, the laser pulse profile is Gaussian.

The envelope model implemented in SMILEI is similar to the one first demonstrated in the PIC code ALaDyn, including the same solver for the envelope equation in laboratory frame coordinates and the ponderomotive solver for the particles’ equations of motion presented in [17,20]. In the following, the equations of this model are presented. Various numerical schemes for their solution are detailed in [20] and those implemented in SMILEI are reviewed in Appendix A. Henceforth, normalized units will be used for all quantities (choosing  $k_0^{-1}$  as the normalized unit length,  $c$  as the normalized unit velocity, etc.).

The fundamental assumption of the model is the description of the laser pulse vector potential in the polarization direction  $\hat{A}(\mathbf{x}, t)$  as a complex slowly varying envelope  $\tilde{A}(\mathbf{x}, t)$  modulated by fast oscillations at wavelength  $\lambda_0$ :

$$\hat{A}(\mathbf{x}, t) = \text{Re} \left[ \tilde{A}(\mathbf{x}, t) e^{i(x-t)} \right], \quad (1)$$

Thus, in general any physical quantity  $Q$  will be therefore given by the summation of a slowly varying part  $\bar{Q}$  and a fast oscillating part  $\hat{Q}$ , i.e.  $Q = \bar{Q} + \hat{Q}$ , where  $\hat{Q}$  has the same structure as in Eq. 1 (we are using the

same notation used in [17]). The laser vector potential in vacuum would have only the fast oscillating part ( $\bar{A} = 0$ ). In this context, “slowly varying” means that the space-temporal variations of  $\bar{A}$  and of the envelope  $\tilde{A}$  of the fast oscillating part are small enough to be treated perturbatively with respect to the ratio  $\epsilon = \lambda_0/\lambda_p$ , as described in detail in [9, 17, 23]. The laser envelope transverse size  $R$  and longitudinal size  $L$  are thus assumed to scale as  $R \approx L \approx \lambda_0/\epsilon$  [9, 23]. As described thoroughly in the same references, the action of the laser envelope on the plasma particles is modeled through the addition of a ponderomotive force term in the particles equations of motion. This term arises from an averaging process in the perturbative treatment of the particles motion over the laser optical cycles [17]. The particles equations of motions (in this case for electrons) thus read:

$$\frac{d\bar{\mathbf{x}}}{dt} = \frac{\bar{\mathbf{p}}}{\bar{\gamma}} \quad (2)$$

$$\frac{d\bar{\mathbf{p}}}{dt} = - \left( \bar{\mathbf{E}} + \frac{\bar{\mathbf{p}}}{\bar{\gamma}} \times \bar{\mathbf{B}} \right) - \frac{1}{\bar{\gamma}} \nabla \Phi \quad (3)$$

$$\bar{\gamma} = \sqrt{1 + |\bar{\mathbf{p}}|^2 + \Phi} \quad (4)$$

where  $\bar{\mathbf{x}}$ ,  $\bar{\mathbf{p}}$ ,  $\bar{\mathbf{E}}$ ,  $\bar{\mathbf{B}}$  are the slow-varying parts of the particles positions and momenta and of the electric and magnetic field. The ponderomotive potential is defined as  $\Phi = |\tilde{A}|^2/2$ . The Lorentz factor in the usual motion equations is replaced by the ponderomotive Lorentz factor  $\bar{\gamma}$  [9, 23]. The quantities stored in an envelope simulation in SMILEI are the slowly varying MP positions and momenta  $\bar{\mathbf{x}}$ ,  $\bar{\mathbf{p}}$ , the slowly varying electromagnetic fields  $\bar{\mathbf{E}}$ ,  $\bar{\mathbf{B}}$ , the envelope  $\tilde{A}$ , the ponderomotive potential  $\Phi$  and its gradient  $\nabla \Phi$ . In a standard laser simulation, the complete (high frequency part and low frequency part) MP positions and momenta  $\mathbf{x}$ ,  $\mathbf{p}$  and electromagnetic fields  $\mathbf{E}$ ,  $\mathbf{B}$  are stored.

The evolution of the laser pulse envelope is derived combining d’Alembert’s inhomogeneous equation and Eq. 1:

$$\nabla^2 \tilde{A} + 2i \left( \partial_x \tilde{A} + \partial_t \tilde{A} \right) - \partial_t^2 \tilde{A} = \chi \tilde{A}. \quad (5)$$

The function  $\chi$  represents the plasma susceptibility, which in a PIC code can be computed similarly to the charge density [13, 20]. This term takes into account the effect of the plasma on the laser propagation, and is necessary to model phenomena of self-focusing [24]. The derivation of Eq. 5 assumes that the high frequency contribution of the scalar potential can be ignored [3, 17].

In SMILEI, no further assumption on the envelope is made and the full form of Eq. 5 is solved. Thus, Eq. 5, solved in ALaDyn and SMILEI, is physically equivalent to the envelope equation in the code INF&RNO (Eq. 1 in [13, 19]), where it is written in comoving coordinates and solved with an implicit numerical scheme detailed in [19]. As explained in [13], we remark that retaining all the terms in the derivation of the envelope equation allows in principle to use this model in conjunction with the Lorentz boosted frame method [11], since the form of Eq. 5 is invariant under Lorentz transformations.

The slowly varying electromagnetic fields  $\bar{\mathbf{E}}$ ,  $\bar{\mathbf{B}}$  are updated solving Maxwell’s equations, with the slowly varying current densities  $\bar{\mathbf{J}}$  as source terms. Since the form of Maxwell’s equations is unaltered, a Finite Difference Time Domain (FDTD) scheme [25] is used to evolve these fields in the simulations described hereafter. The deposition of  $\bar{\mathbf{J}}$  is performed with the charge conserving scheme by Esirkepov [26].

Modeling the laser through a complex envelope and its coupling with the plasma through the ponderomotive force will yield physically meaningful results only if the variation scales in space and time are greater than  $\lambda_0$ ,  $1/\omega_0$ . Examples violating these hypotheses include, but are not limited to, tightly focused lasers and few optical cycles lasers. Thus, although the simulations described in the following use Gaussian temporal and transverse profiles for the laser pulse, different and even more realistic profiles can be simulated through the envelope model, provided that their spatial and temporal variations are not too steep. In the case of few cycle pulses injected in plasmas, where carrier envelope phase effects are important, the envelope model cannot catch these phenomena with spatial and temporal variations scales smaller than  $\lambda_0$  and  $1/\omega_0$ .

### 3. Benchmark case study: second stage simulations

An envisioned experiment for Apollon is the injection of electrons from a first nonlinear plasma stage and their transport line towards a second plasma stage (which could be created for example through a capillary discharge or a laser formed channel [27]), where they will be accelerated by plasma waves in the weakly nonlinear regime. The lower accelerating gradients of weakly nonlinear regimes imply the requirement of a large accelerating length for the second plasma stage to have a substantial energy gain. This represents a considerable challenge from the experimental point of view, but also for the numerical simulation, which would be unfeasible with a standard laser simulation techniques. In order to demonstrate the suitability of the envelope model for second stage simulations, we report a comparison between a standard laser and an envelope simulation. The physical setup is given by a laser pulse injected in a plasma

and an idealized Gaussian electron beam injected from outside the plasma, as for an external injection experiment into a second stage. The ideal laser, plasma and beam parameters are the same as in [28] and are briefly recalled in the following.

The Gaussian laser pulse, linearly polarized in the  $y$  direction, has a waist size  $w_0 = 45 \mu\text{m}$ . Its Gaussian temporal profile has an initial FWHM duration  $\tau_0 = 108$  fs in intensity and peak normalized field amplitude  $a_0 = \sqrt{2}$ . The idealized plasma profile is given by a transversely parabolic profile  $n_e(r) = n_0 \left(1 + \frac{\Delta n}{n_0} \frac{r^2}{r_0^2}\right)$  (with  $r$  the distance to axis,  $n_0 = 1.5 \cdot 10^{17} \text{ cm}^{-3}$ ,  $\frac{\Delta n}{n_0} = 0.25$ ,  $r_0 = 45 \mu\text{m}$ ), starting from the initial right boundary of the moving window, which has longitudinal and transverse dimensions  $L_x = 1400 k_0^{-1}$  and  $L_y = L_z = 1600 k_0^{-1}$ . The laser is focused at the beginning of the plasma profile, and its initial center is chosen at a distance  $2\sqrt{2} \tau_0$  from the plasma. The longitudinal cell size for the standard laser simulation is  $\Delta x_{\text{laser}} = 0.196 k_0^{-1}$  and the transverse cell size is  $\Delta y = \Delta z = 3 k_0^{-1}$ . The time step has been chosen as  $\Delta t_{\text{laser}} = 0.95 \Delta x_{\text{laser}}$ . For the envelope simulation, the longitudinal grid cell size and the integration time step have been set to  $\Delta x_{\text{envelope}} = 16 \Delta x_{\text{laser}}$ ,  $\Delta t_{\text{envelope}} = 0.8 \Delta x_{\text{envelope}}$  respectively. In both the simulations, 8 particles per cell have been used.

According to our tests, the larger longitudinal cell size and integration timestep in the envelope simulation seed the numerical Cherenkov radiation (NCR) more quickly than in the standard laser simulations, as expected from the underlying theory [29]. This numerical artifact has detrimental effects on the beam emittance after long propagation distances. To partially cope with the NCR, we use a binomial filter (2 passes) on the current densities at each iteration [30]. The binomial filter in one dimension (without compensator) is defined as  $Q_i^f = \frac{1}{2}[Q_i + \frac{1}{2}(Q_{i-1} + Q_{i+1})]$ , where  $Q^f$  is the result of the application of the binomial filter on the quantity  $Q$  and  $i$  is the grid index in one direction. Efficient binomial filtering in two and three dimensions is obtained re-applying the filter on the other directions [6]. An advantage of the envelope model, as well as of boosted frame simulations as explained in [30], is that the laser is not modeled with high frequency oscillations, so low-pass filtering does not risk to damp the high frequency phenomena close to the laser as it would do in a standard laser simulation [30]. Therefore, in the standard laser simulation no low-pass filter is used.

As it will be shown in the following, another advantage of the envelope model compared to the FDTD scheme is a more correct description of the laser propagation velocity [20]. As pointed out in [17], a numerically slowed laser implies a numerically exaggerated dephasing phenomenon, i.e. the accelerated bunch exits the accelerating wakefield behind the laser at an unphysically earlier time. This has important consequences on the predicted energy and energy spread, since this phenomenon places the bunch in an unphysical phase of the wakefield during the acceleration process. Although the envelope model does not completely remove this numerical artifact, its effect is less significant than in the case of a laser evolved through a FDTD solver with standard resolution.

The electron beam injected after the laser has an ideal Gaussian density profile in all the phase space sub-planes and a total charge of  $Q = 30$  pC. Its mean energy is 150 MeV, with a 0.5% rms energy spread. The beam transverse rms size is  $1.3 \mu\text{m}$ , its longitudinal rms size  $2 \mu\text{m}$ , with a transverse normalized emittance of 1 mm-mrad. The beam initial position is at a distance  $0.75\lambda_p$  after the laser pulse, in a phase with both a focusing and an accelerating field in the wake of the laser in the plasma. All the electron beam MP carry the same electric charge, given by  $Q/N_p$ , where  $N_p = 10^6$  is the number of MP which sample the beam. To self-consistently initialize the EM fields of an electron beam that is already relativistic at the beginning of the simulation, the procedure described in [31, 32] was implemented in SMILEI. To summarize, at the beginning of the simulation the ‘‘relativistic Poisson’s equation’’ is solved, once the initial beam charge density  $\bar{\rho}$  is computed:

$$\left(\frac{1}{\gamma_0^2} \partial_x^2 + \nabla_{\perp}^2\right) \bar{\Phi} = -\bar{\rho}. \quad (6)$$

Then, the low frequency EM fields  $\bar{\mathbf{E}}$ ,  $\bar{\mathbf{B}}$  at the same time step  $t = 0$  are computed:

$$\bar{\mathbf{E}} = \left(-\frac{1}{\gamma_0^2} \partial_x, -\partial_y, -\partial_z\right) \bar{\Phi}, \quad (7)$$

$$\bar{\mathbf{B}} = \beta_0 \hat{\mathbf{x}} \times \bar{\mathbf{E}}. \quad (8)$$

The quantities  $\gamma_0 = 1/\sqrt{1 - \beta_0^2}$  and  $\beta_0$  represent the initial mean beam Lorentz factor and initial normalized speed respectively. The quantities  $\bar{\rho}$  and  $\bar{\Phi}$  are centered on the primal grid in all the  $x$ ,  $y$ ,  $z$  directions. The derivatives in the previous equations are computed through finite differences. In order to provide the properly space-centered fields for the FDTD scheme, the magnetic field is then spatially interpolated in the Yee cell. Besides, in order to provide the properly time-centered initial conditions for the FDTD scheme, the magnetic field at time  $-\Delta t/2$  is found using a backward FDTD ‘‘advance’’ by  $-\Delta t/2$ . Silver-Müller boundary conditions for the electromagnetic fields [33, 34] have been used in the simulations. Although they are not ideal to absorb the field of a relativistic electron beam (absorbing boundary conditions as in [35] would be more suited), our simulation domain was sufficiently large to

damp enough the fields at the transverse boundaries and the spurious remaining reflections were screened by the plasma.

Table 1 reports the electron beam parameters obtained by the two simulations after a propagation distance of 15 mm. We note a very good agreement for certain parameters as the mean energy, the transported charge and the beam duration after this distance. The most striking differences are found in the energy spread and in the transverse plane parameters as the rms sizes  $\sigma_i$  ( $i = y, z$ ) and normalized emittances  $\varepsilon_{n,i}$ . The normalized emittance is defined as  $\varepsilon_{n,i} = \sqrt{\sigma_i^2 \sigma_{p_i}^2 - \sigma_{ip_i}^2}$  ( $i = y, z$ ), where  $\sigma_{p_i}$  and  $\sigma_{ip_i}$  are the beam rms momentum spread and covariance between the coordinate  $i$  and the momentum  $p_i$  in the transverse planes  $y - p_y$  and  $z - p_z$ .

Figure 6 reports the phase space distribution of the beam in the transverse  $y - p_y$  plane after 15 mm. A similar distribution is found in the transverse  $z - p_z$  plane. In this Figure, the smaller final emittance predicted by the envelope simulation, already reported in Table 1, becomes evident. The differences in the beam emittance, which is conserved along the propagation in the envelope simulation, is mainly due to the mitigation of NCR thanks to the smoothing operated on the current density. The possibility of low-pass filtering, and thus reduction of the effects of this numerical artifact plaguing standard LWFA PIC simulations, without compromising the laser propagation represents an important advantage of envelope simulations. PIC simulations of LWFA not using envelope need more advanced techniques to cope with NCR, like *ad-hoc* solvers for Maxwell's Equations [29, 36, 37] instead of the FDTD solver, or pseudo-spectral electromagnetic solvers [38] coupled to the Galilean coordinates method in boosted frame simulations as described in [39, 40].

The differences in energy can be explained with the abovementioned greater numerical dephasing of the FDTD, which numerically slows down the laser pulse more than how the envelope equation solver does. To illustrate this phenomenon, we report in Figs. 2,3 a comparison between the two simulations at 3.7 mm. A good agreement can be seen in the predicted longitudinal electric field and the electron density. The same comparison at 15 mm is reported in Figs. 4, 5, where the difference in the numerical propagation of the laser predicted by the two simulations can be seen. From Fig. 4, where the longitudinal electric field on axis is compared at 15 mm, it is evident that the laser pulse is moving faster in the envelope simulation, and after a long simulation time the difference in the traveled distance becomes sensitive. Instead, the electron beam moves at the same velocity (close to  $c$ ) in both simulations and is found at the same position (see Fig. 5) at the same simulation time. Thus, the electron beam is subject to a numerically exaggerated dephasing in the standard laser simulation. As can be seen from Fig. 4, the beam loading is sensitive to the different wakefield phases where the electron beam is found in the two simulations, where the laser propagates at different speed. These differences in beam loading and in dephasing yield a lower energy and a lower energy spread in the standard laser simulation, clearly visible in the longitudinal phase space distribution (Fig. 7).

To summarize, in these particular conditions the simulation of the second stage can greatly benefit from a modeling based on the envelope approximation. Compared to standard laser simulations, calculations using laser envelopes can use digital filters to cope with NCR without damping the relevant physics near the laser and the reduced numerical dispersion can yield more accurate results. Besides, the envelope simulations only need a fraction (5% in this case) of the computing resources required by a standard laser simulation. The necessary computing resources for this simulation up to 15 mm with a standard laser are not easily available normally and were provided by the Grand Challenge "Irene" 2018 project of GENCI.

A realistic second stage in the weakly nonlinear regime would be much longer than 15 mm and near to the laser depletion length. In [17, 19] for example, propagation distances longer than one centimeter are modeled through an envelope model. The propagation distance of the results we described is much smaller than the depletion length of the laser, where the laser envelope starts to be significantly deformed [19]. The simplest approach to resolve the small scale structures which develop in the laser envelope at those distances would be to use a finer resolution. However, this would reduce the envelope model rapidity, its main advantage over standard codes. There are alternative techniques to correctly model laser depletion without using high resolutions and thus retaining the envelope speedup, for example the discretization approach described in [19]. At the moment no technique of this kind is implemented in SMILEI. As explained in the same reference, retaining the second time derivative in the envelope equation (like in Eq. 5) is a necessary condition to model laser depletion. Thus, in the future similar techniques could be developed in the code as a development of the presented envelope equation solver in principle.

#### 4. Single stage simulations for Apollon

This Section illustrates the interest of the envelope model to run simulation campaigns applied to real experimental setups.

In Section 3, we have compared the results of a standard laser simulation and an envelope simulation for a long distance LWFA benchmark in a weakly nonlinear regime. Examples of the use of time explicit envelope models for

	Initial values	Standard Laser (15 mm)	Envelope (15 mm)
$Q$ (pC)	30	29.98	29.94
$\sigma_x$ ( $\mu\text{m}$ )	2.0	2.0	2.0
$\sigma_y$ ( $\mu\text{m}$ )	1.3	1.5	1.0
$\sigma_z$ ( $\mu\text{m}$ )	1.3	1.4	1.0
$\varepsilon_{n,y}$ (mm-mrad)	1.0	2.0	1.0
$\varepsilon_{n,z}$ (mm-mrad)	1.0	2.1	1.0
$E$ (MeV)	150	427	438
$\sigma_E/E$ (%)	0.5	4.7	6.4

Table 1: Beam parameters: charge  $Q$ , rms sizes  $\sigma_i$  ( $i = x, y, z$ ), normalized emittances  $\varepsilon_{n,i}$  ( $i = y, z$ ), mean energy  $E$ , rms energy spread  $\sigma_E/E$ . First column: beam parameters at the beginning of the simulation. Second and third columns: beam parameters after 15 mm of propagation in the standard laser simulation and envelope simulation.

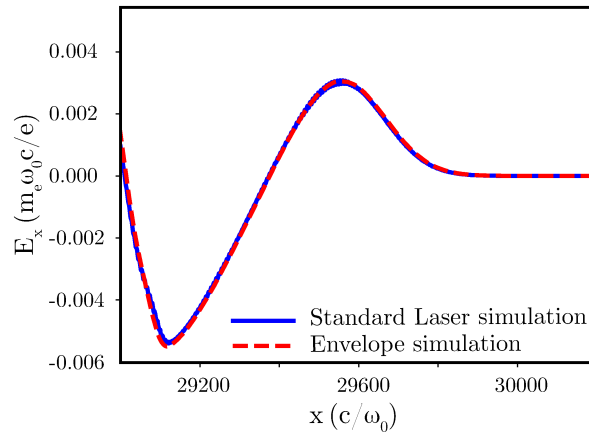


Figure 2: Longitudinal electric field  $E_x$  on axis after 3.7 mm of propagation, comparing the results obtained with the envelope model and the results obtained through a standard laser simulation.

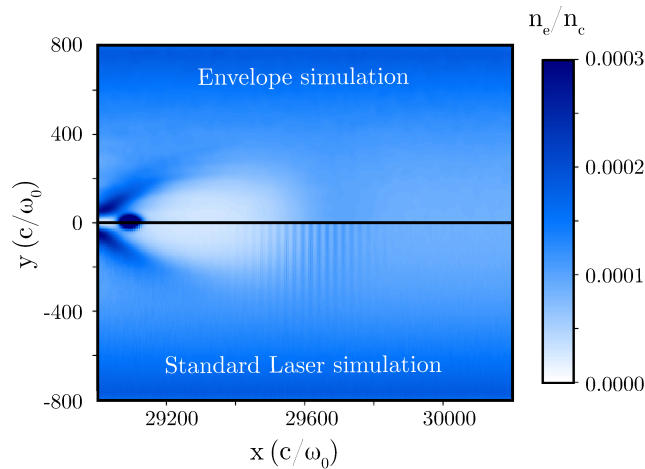


Figure 3: Plasma density after 3.7 mm of propagation. Top panel: results obtained with the envelope model. Bottom panel: results obtained through a standard laser simulation.

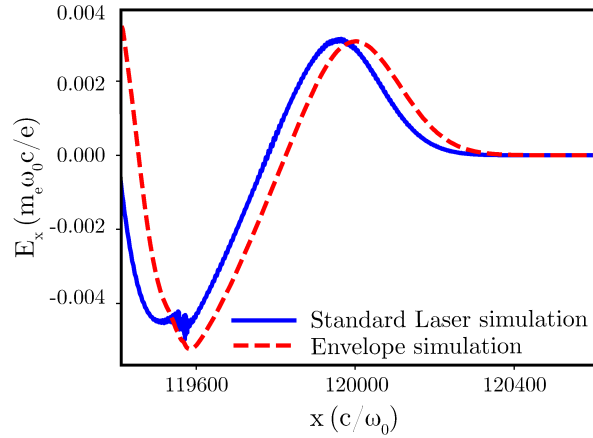


Figure 4: Longitudinal electric field  $E_x$  on axis after 15 mm of propagation, comparing the results obtained with the envelope model and the results obtained through a standard laser simulation.

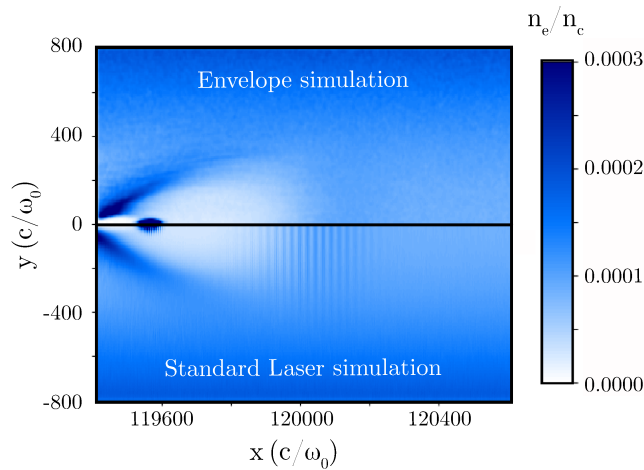


Figure 5: Plasma density after 15 mm of propagation. Top panel: results obtained with the envelope model. Bottom panel: results obtained through a standard laser simulation.

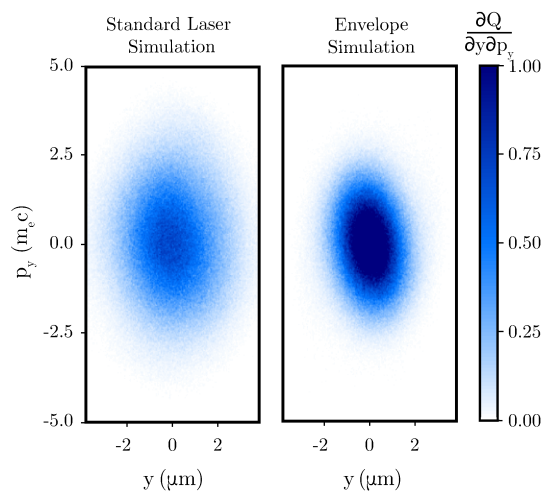


Figure 6: Normalized  $y - p_y$  phase space distribution of the externally injected and LWFA-accelerated electron beam after a propagation distance of 15 mm.



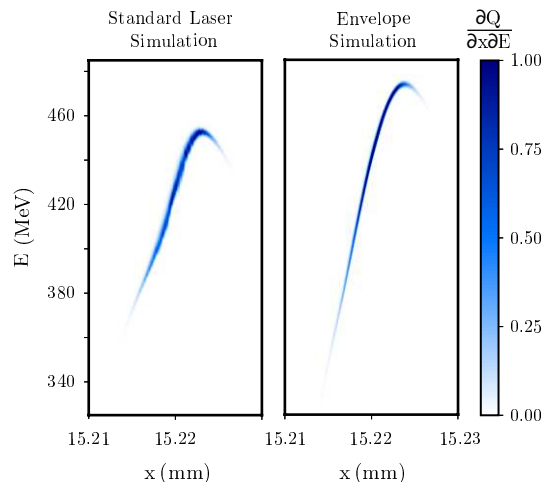


Figure 7: Normalized longitudinal phase space distribution of the externally injected and LWFA-accelerated electron beam after a propagation distance of 15 mm.

highly nonlinear regimes with self-injection, like those discussed in this Section, can be found for example in [12, 17].

A set of four 3D simulations is performed in order to probe the parameter space accessible to the first Apollon shots. These simulations represent a potential experimental setup using a supersonic gas jet, where the electrons would be injected and accelerated to high energies in a single plasma stage. The very first experiments will be done with increasing laser energy starting from 5 J and up to 15 J. We expect the laser pulse duration to be between 20 and 30 fs. In order to fix parameters for a simple single stage LWFA experiment within this window of laser pulse energy and length, one can use the criteria defined in [41]. The plasma density window is limited by the diffraction-limited propagation on one side  $\omega_p \tau_L \geq 1$ , and the depletion-limited propagation on the other  $\omega_p \tau_L \leq \pi/2$ . And once a density is chosen, the minimum power is  $P_- = 10P_{cr}$  in order for the relativistic self-focusing to counter balance diffraction. We remind that  $P_{cr} = 16.2(n_c/n_0)$  GW, where  $n_0$  and  $n_c$  are respectively the electron and critical density respectively [24]. The laser wavelength is  $\lambda_0 = 0.8 \mu\text{m}$ . The maximum power is  $P_+ = 25P_{cr}$  in order to stay in the self-guided propagation without critical oscillations of the laser spot size. The laser pulse length being already fixed, the criteria on  $P$  translates directly into a condition on the energy. This is illustrated in Fig. 8 which shows, for different pulse lengths, the minimum and maximum energy as a function of density within the prescribed density window. It is worthwhile to note that, as the pulse becomes shorter in time, the energy window narrows and the optimal energy decreases. Future high energy LWFA experiments based on a similar self-guided laser pulse willing to reach high charges or energy should therefore make use of longer laser pulses.

The Gaussian laser pulse is focused at the start of the plasma, with a waist size  $w_0 = 40 \mu\text{m}$ . This is the waist of a Gaussian function that fits the central disk of the Airy pattern of a top-hat beam of diameter focused at  $f/64$ . This corresponds to the Apollon F2 beam of diameter  $D = 140$  mm, focused with a mirror of focal length  $f = 9$  m. With a laser wavelength  $\lambda_0 = 0.8 \mu\text{m}$ , the corresponding Rayleigh length in vacuum would be  $\approx 6.3$  mm, but relativistic self-focusing allows to guide the laser for a longer distance. The plasma density of all the simulations was defined with a  $300 \mu\text{m}$  upramp from 0 to the plateau density value  $n_0$ , reported in Table 2. After the upramp, the plasma density remains constant. Besides, the plasma density is chosen uniform in the transverse direction, to rely only on relativistic self-focusing for the laser guiding [24]. In all the scan simulations, 8 particles per cell have been used. The integration timestep was always set to  $\Delta t = 0.9 \Delta x$ , where  $\Delta x$  is the longitudinal mesh cell size. The transverse mesh cell size has been set to  $\Delta y = \Delta z = 3.5 k_0^{-1}$  for all the simulations. As in the simulations reported in Section 3, we used a binomial filter on the current densities at each iteration (2 passes). Again, this smoothing aims at limiting the NCR impact on the simulation.

We remark that a similar set of equivalent 3D simulations would have been unfeasible with standard laser simulations. For reader's convenience, the parameters of the four simulations have been summarized in table 2, including the longitudinal mesh cell size.

Figure 9 (top left panel) depicts the evolution of the peak absolute value of the electric field envelope  $|\tilde{E}|$  for the four simulations. From the definition of the envelope  $\tilde{A}$  of the vector potential  $\hat{A}$  along the polarization direction (Eq. 1), this quantity is defined as the amplitude of the envelope of  $\tilde{E} = -\partial_t \tilde{A}$ , i.e.  $\tilde{E} = -(\partial_t - i)\tilde{A}$ . As desired, the ratios  $P/P_{cr} \gg 1$  lead to relativistic self-focusing [24], which suddenly enlarges the bubble behind the laser, triggering electron injection. The importance of dark current (low energy tail in electrons energy distribution) depends strongly

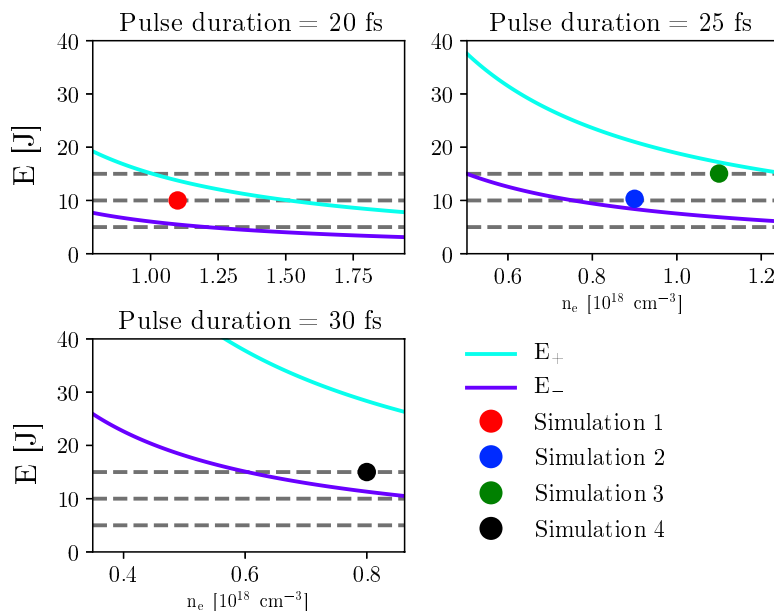


Figure 8: Density window prescribed by pulse length. Minimum energy  $E_-$  and maximum energy  $E_+$  in order to guarantee proper self-focusing and propagation are plotted as functions of the plasma density. The plasma density ranges between  $n_-$ , in order to have self-focusing effectively counter-balancing diffraction, and  $n_+$  above which laser depletion makes the acceleration inefficient and unstable. Optimum parameters are located at the center of the delimited zone. Accessible parameters with energies of 5, 10 and 15 J are plotted as gray dashed lines. Colored dots mark the parameters chosen for the scan simulations.

Simulation	Pulse duration [fs]	$a_0$	$n_0$ [ $10^{18} \text{ cm}^{-3}$ ]	$P/P_{cr}$	Laser Energy [J]	$\Delta x$ [ $k_0^{-1}$ ]
1	20	2.96	1.1	18.3	10	0.5
2	25	2.64	0.9	12.0	10	0.667
3	25	3.24	1.1	22.0	15	0.667
4	30	2.96	0.8	13.3	15	0.8

Table 2: Laser and Plasma Parameters for the scan simulations. The waist size has been chosen as  $40 \mu\text{m}$  for all the four simulations. The laser strength parameter [3] is denoted by  $a_0$ . The longitudinal mesh cell size  $\Delta x$  is also reported. The transverse mesh cell size has been set to  $\Delta y = \Delta z = 3.5 k_0^{-1}$  and the integration timestep to  $\Delta t = 0.9 \Delta x$ .

on the set of parameters used. An *ad hoc* definition of the beam is used here in order to separate it from the dark current when necessary.

After injection, the energy distribution of the electrons shows a distinct peak at  $E_{\text{spectrum peak}}$  and a full width half maximum  $\Delta E$ . We define the injected beam, at a given time, as the electrons having an energy within an interval of width  $2\Delta E$  around  $E_{\text{spectrum peak}}$ .

Figure 9 also shows the evolution of the total charge  $Q_{\text{tot}}$  above 300 MeV (bottom left panel) and the energy of the spectrum peak  $E_{\text{spectrum peak}}$  (top right panel). As in [41] (where the same regime is simulated), self-focusing of the laser triggers self-injection in our simulations. Since secondary injections can create additional peaks in the electron spectrum, the energy of the peak  $E_{\text{spectrum peak}}$  can vary suddenly when a peak overtakes another one and becomes the new maximum of the distribution (see red line or green line of the top right panel in Figure 9).

The evolution of the laser due to self-focusing changes the length of the bubble during injection, which also modifies the length of the bubble due to beam loading. These results yield a nonlinear evolution of the beam, which can be found in different phases of the longitudinal wakefield during the acceleration process. As example, we report in Fig. 10 the evolution of the energy spectrum in simulation 1. From the Figure we note that the electrons injected first (around 3 mm), the head of the first injected beam, have an energy greater than the particles injected for

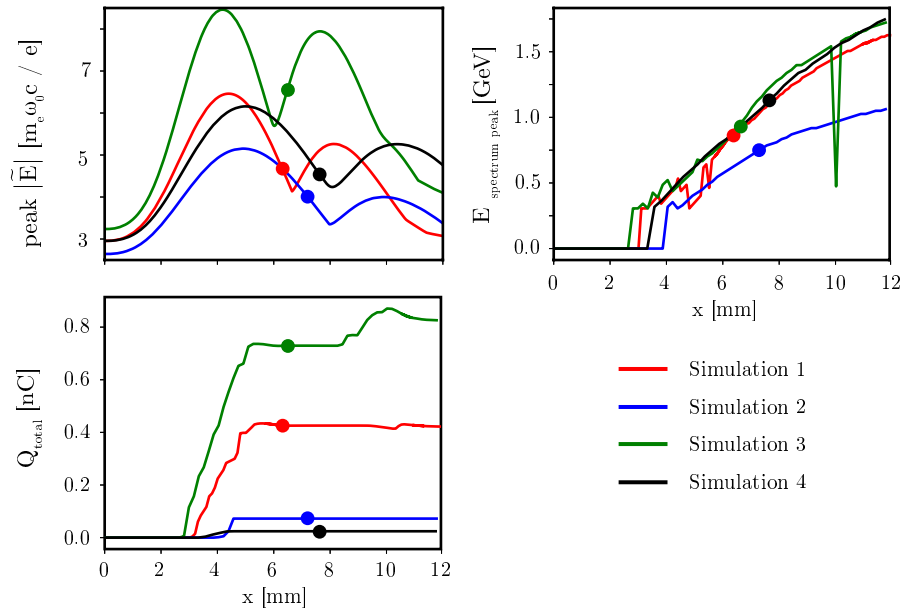


Figure 9: Top left panel: Evolution of the absolute value of the laser peak electric field envelope  $|\tilde{E}|$ . Top right panel: evolution of the energy of the electron spectrum peak  $E_{\text{spectrum peak}}$  for particles with energy above 300 MeV. Bottom left panel: Evolution of the the total charge  $Q_{\text{tot}}$  above 300 MeV. In all the panels, the colored markers highlight the “optimum” laser propagation distance, before the electron beam starts its rotation in the longitudinal phase space

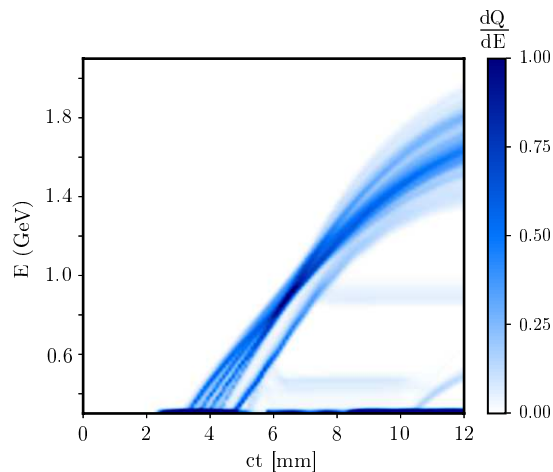


Figure 10: Evolution of the energy distribution during the injection and acceleration process in the simulation 1. The charge spectral density has been normalized. The horizontal axis is the simulation time  $t$ , multiplied by the speed of light  $c$ .

example around 4 mm, in the tail of the first beam, until a point where the ordering in energy starts to reverse, around 6 mm. We can also see that the energy gain of the particles per unit distance starts to decrease, due to the beam approaching the turning point of the longitudinal wakefield (i.e. the dephasing starts [43]). The other simulations yield a similar behavior for the beam energy distribution, albeit for example with a lower energy spread in the case of simulation 4. To provide interesting working points for the Apollon experiments, in Table 3 we report the injected beam parameters after a certain laser propagation distance, different for each simulation. This optimal distance has been chosen by carefully following the evolution of the injected beam spectrum. At that point, the electron beam reaches the maximum spectral density (6.3 mm in simulation 1, visible in in Fig. 10). It corresponds to the moment when phase space rotation minimizes the beam energy spread [43]. As seen on Fig. 9, the acceleration process goes on past this point but at the cost of a reduced beam quality and possible additional dark current. For all the simulations, this optimal propagation distance is found around 6-7 mm. In all these working points, the spectrum peak energy is around 1 GeV, with an energy spread lower than 10%. Fig. 11 reports the electron energy spectrum for all the simulations at this “optimum” laser propagation distance.

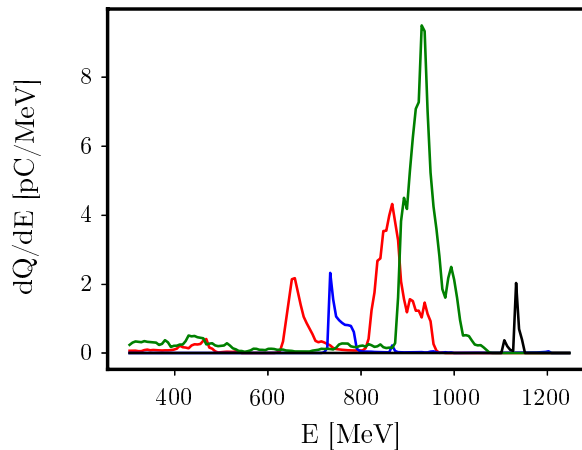
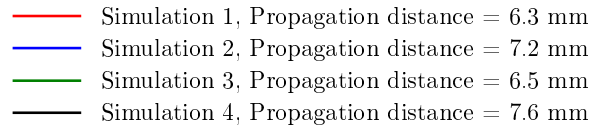


Figure 11: Energy spectrum of the single stage simulations at the “optimum” laser propagation distance. The cut-off energy is 300 MeV.

Even in the relatively well constrained range of parameters, significant differences are observed. First, there is a factor 20 between the minimum and maximum beam charges. This parameter appears to be controlled primarily by the  $P/P_{cr}$  ratio. Lasers close to the  $P/P_{cr} = 10$  are subject to milder self-focusing and trigger less self-injection (simulations 2 and 4). Conversely, for higher  $P/P_{cr}$ , self-injection is dramatically enhanced (simulations 1 and 3). This dependency is expected [41] and provides a practical way to optically control the injected charge even though the sensitivity is such that it might be difficult to achieve a very good accuracy.

The energy evolution is roughly similar in all cases with the exception of simulation 2. This evolution is governed by the accelerating field  $E_{acc}$ . In the bubble regime,  $E_{acc}$  is proportional to  $\sqrt{a_0 n_0}$  [3]. In the simulations,  $n_0$  is constant and therefore,  $a_0$  evolution dictates the evolution of the accelerating field. This evolution is shown as the normalized peak  $|\tilde{E}|$  in figure 9. Simulation 2 has a small density and the weakest  $a_0$  throughout the run because of a low initial  $a_0$  but also the weakest self-focusing. This explains the small acceleration observed in that case with respect to the other simulations. Simulation 4, performs quite well in terms of acceleration in spite of having the smallest density and only a medium initial  $a_0$  thanks to a superior laser guiding. Simulation 3, in spite of having the highest  $a_0$  and density do not outperform other simulations in terms of energy because in that case the beam loading effect is not negligible anymore [44].

The computing time needed by the 3D simulations for 1 mm is of the order of 30-60 kh. We remark that a parameter scan of four 12 mm long 3D simulations as the one presented in this work would have been extremely costly with standard laser simulations, which are typically slower by at least a factor 20. This justifies the interest in time-explicit envelope models [13, 17], especially for preliminary studies for experiments like those planned for

Simulation	1	2	3	4
$n_0$ [ $10^{18}$ cm $^{-3}$ ]	1.1	0.9	1.1	0.8
$a_0$	2.96	2.64	3.24	2.96
$P/P_{cr}$	18.3	12.0	22.0	13.3
Laser Energy [J]	10	10	15	15
Pulse duration [fs]	20	25	25	30
Laser propagation distance [mm]	6.3	7.2	6.5	7.6
$Q_{beam}$ [pC]	263	48	543	24
$Q_{total, >300 MeV}$ [pC]	426	72	729	24
$E_{spectrum\ peak}$ [MeV]	870	740	930	1130
$\Delta E/E_{spectrum\ peak}$ [%]	8.3	3.2	6.4	2.0
$2\sigma_y$ [ $\mu\text{m}$ ]	3.0	2.3	2.9	0.5
$2\sigma_z$ [ $\mu\text{m}$ ]	2.8	2.3	3.1	0.5
$\varepsilon_{n,y}$ [mm-mrad]	14.5	1.3	12.3	0.4
$\varepsilon_{n,z}$ [mm-mrad]	11.8	1.3	13.1	0.4

Table 3: Resume of the plasma plateau density  $n_0$ , initial laser pulse parameters used in the set of first stage simulations. For the electron beam, the peak in the energy spectrum  $E_{spectrum\ peak}$ , the relative energy spread  $\Delta E/E_{spectrum\ peak}$ , rms size (2 standard deviations  $\sigma$ ) and the normalized emittances  $\varepsilon_{n,i}$  ( $i = y, z$ ) in the transverse planes are reported. These parameters are measured after a certain laser propagation distance, before the phase space rotation, reported in the table.

Apollon.

## 5. Conclusions

A recently published, time explicit, easily parallelizable envelope method for PIC codes has the potential to model laser-plasma interaction involved in many LWFA setups with considerable speedups compared to standard laser simulations. The implementation of this time-explicit model in SMILEI has been described. The suitability of this envelope model for single-stage with self-injection and second-stage LWFA simulations has been explored. The laser and plasma parameters chosen for these studies lie within the intervals of interest for the upcoming Apollon LWFA experiments.

The envelope model used in this work has been benchmarked against a standard laser simulation in a scenario with external injection of a witness electron beam, yielding a speedup of 20 compared to a standard laser simulation and a good agreement even at a distance of 15 mm. Besides, the envelope model allows to model more accurately the longitudinal and transverse phase space evolution of the injected beam. Indeed, in the longitudinal direction a more accurate prediction of the laser propagation speed by the envelope equation reduces the numerical dephasing of the electron beam caused by FDTD solvers of Maxwell's equations. In the transverse direction, the envelope simulations allow for low-pass filtering which in this case considerably reduced the growth of NCR, conserving the beam emittance.

In the single-stage simulations, four potential working points in the regions of parameters of interest have been tested, finding the injection of  $\approx 1$  GeV electron beams with energy spread lower than 10%. These working points have been found examining the evolution of the injection and acceleration process for 12 mm in four 3D simulation, a propagation distance which would need considerable computing resources to be simulated with a standard 3D PIC code.

The use of this envelope model may thus represent an important investigation tool for the study of LWFA and parameter explorations with reduced resource requirements. Further improvements could include spectral solvers for the envelope equation and Maxwell's equations to cope with numerical Cherenkov radiation and the use of cylindrical symmetry to speed up even further the simulations (albeit losing the full 3D characteristics of the phenomena).

## Appendix A. Envelope PIC loop

We report a brief summary of the numerical solution of the equations involved in the envelope model used for the simulations of this work. More details on the derivation of the equations and the numerical schemes used to solve

1  
2 them can be found in [20]. The envelope equation that SMILEI solves is

$$3 \quad \nabla^2 \tilde{A} + 2i \left( \partial_x \tilde{A} + \partial_t \tilde{A} \right) - \partial_t^2 \tilde{A} = \chi \tilde{A}, \quad (\text{A.1})$$

4  
5 in which the the susceptibility  $\chi$  is defined as

$$6 \quad \chi(\mathbf{x}) = \sum_s r_s^2 \sum_p \frac{w_p}{\bar{\gamma}_p} S(\mathbf{x} - \bar{\mathbf{x}}_p), \quad (\text{A.2})$$

7  
8 where  $\bar{\gamma}_p$  is the averaged or ponderomotive Lorentz factor of the macroparticle  $p$  and  $r_s = q_s/m_s$  is the charge to  
9 mass ratio ( $q_s$  and  $m_s$  are respectively the particle species  $s$  charge and mass normalized by the elementary charge  
10  $e$  and electron mass  $m_e$ ). The MP weight and shape factor are denoted by  $w_p$  and  $S(\mathbf{x})$  respectively (see [6] for the  
11 definition of shape factor). The averaged Lorentz factor is defined from the averaged particle momentum  $\bar{\mathbf{u}}_p = \bar{\mathbf{p}}_p/m_s$   
12 and the ponderomotive potential  $\Phi = |\tilde{A}|^2/2$  [9, 17, 23]:

$$13 \quad \bar{\gamma}_p = \sqrt{1 + \bar{\mathbf{u}}_p \cdot \bar{\mathbf{u}}_p + r_s^2 \Phi(\bar{\mathbf{x}}_p)}. \quad (\text{A.3})$$

14  
15 Maxwell's equations retain their form, except for substituting the electromagnetic fields and the source terms  
16 with their respective low frequency components (denoted with a bar):

$$17 \quad \partial_t \bar{\mathbf{E}} = \nabla \times \bar{\mathbf{B}} - \bar{\mathbf{J}} \quad (\text{A.4})$$

$$18 \quad \partial_t \bar{\mathbf{B}} = -\nabla \times \bar{\mathbf{E}}. \quad (\text{A.5})$$

19  
20 The low frequency current density  $\bar{\mathbf{J}}$  is projected on the grid through Esirkepov's method [26].

21  
22 Also the MP equations of motion remain similar to the usual ones, but with a crucial difference: the low frequency  
23 components of the position and momentum are pushed by both the low frequency electromagnetic fields (the Lorentz  
24 force term) and the ponderomotive force  $\mathbf{F}_{pond} = -r_s^2 \frac{1}{4\bar{\gamma}_p} \nabla \Phi$ . This term takes into account the averaged effect of  
25 the laser on the particles and can be computed from the envelope  $\tilde{A}$ . The resulting equations of motions for the  
26 particle of index  $p$  are:

$$27 \quad \frac{d\bar{\mathbf{x}}_p}{dt} = \frac{\bar{\mathbf{u}}_p}{\bar{\gamma}_p} \quad (\text{A.6})$$

$$28 \quad \frac{d\bar{\mathbf{u}}_p}{dt} = r_s \left( \bar{\mathbf{E}}_p + \frac{\bar{\mathbf{u}}_p}{\bar{\gamma}_p} \times \bar{\mathbf{B}}_p \right) - r_s^2 \frac{1}{4\bar{\gamma}_p} \nabla \Phi_p. \quad (\text{A.7})$$

29  
30 The nonlinearities introduced in the envelope source term (Eqs. A.2,A.3) and the ponderomotive force by the  
31 terms  $\bar{\gamma}$  (Eq. A.3) and  $\nabla \Phi$  require a modification of the standard PIC algorithm. The PIC loop is changed to  
32 implement the solution of the ponderomotive equations (Eqs. A.1,A.6), adding the envelope equation solver, the  
33 susceptibility deposition and a ponderomotive particle push, as depicted in Fig.A1.

34  
35 The interpolation of the fields to the MP positions and the deposition of the current density and susceptibility  
36 on the grid are implemented as in standard PIC codes [6]. In the simulations presented in this work, we used an  
37 order 2 shape function, without loss of generality.

38  
39 As explained in detail in [20], Eq. 5 can be discretized using finite differences both in time and space. The  
40 second order centered finite differences yield an explicit scheme:

$$41 \quad \tilde{A}_{ijk}^{n+1} = \frac{1 + i\Delta t}{1 + \Delta t^2} \left[ 2\tilde{A}_{ijk}^n - (1 + i\Delta t)\tilde{A}_{ijk}^{n-1} + \left( \nabla^2 \tilde{A} \Big|_{ijk}^n - \chi_{ijk}^n \tilde{A}_{ijk}^n + 2i\Delta t^2 \frac{\tilde{A}_{i+1jk}^n - \tilde{A}_{i-1jk}^n}{2\Delta x} \right) \right] \quad (\text{A.8})$$

42  
43 where

$$44 \quad \nabla^2 \tilde{A} \Big|_{ijk}^n = \frac{\tilde{A}_{i+1jk}^n - 2\tilde{A}_{ijk}^n + \tilde{A}_{i-1jk}^n}{\Delta x^2} + \frac{\tilde{A}_{ij-1k}^n - 2\tilde{A}_{ijk}^n + \tilde{A}_{ij+1k}^n}{\Delta y^2} + \frac{\tilde{A}_{ijk-1}^n - 2\tilde{A}_{ijk}^n + \tilde{A}_{ijk+1}^n}{\Delta z^2}. \quad (\text{A.9})$$

45  
46 The indices  $i, j, k$  refer to the mesh cell indices along the  $x, y, z$  directions. The envelope, the ponderomotive potential  
47 and the susceptibility are centered in space as the charge density in all directions and time-centered as the electric  
48 field in the Yee scheme [25].

49  
50 Once the susceptibility term at time step  $n$  is known, the past and present envelope fields ( $\tilde{A}^{n-1}$ ,  $\tilde{A}^n$  respectively)  
51 can be used to compute  $\tilde{A}^{n+1}$  using Eq. A.8. The stencil of this explicit envelope solver contains three points in  
52 space for each direction.

53  
54 To project the susceptibility on the grid and to update the MP momenta, as explained in [20], the ponderomotive  
55 Lorentz factor at the timestep  $n$  is necessary. This quantity cannot be directly computed from Eq. A.3, since the  
56  
57  
58  
59  
60

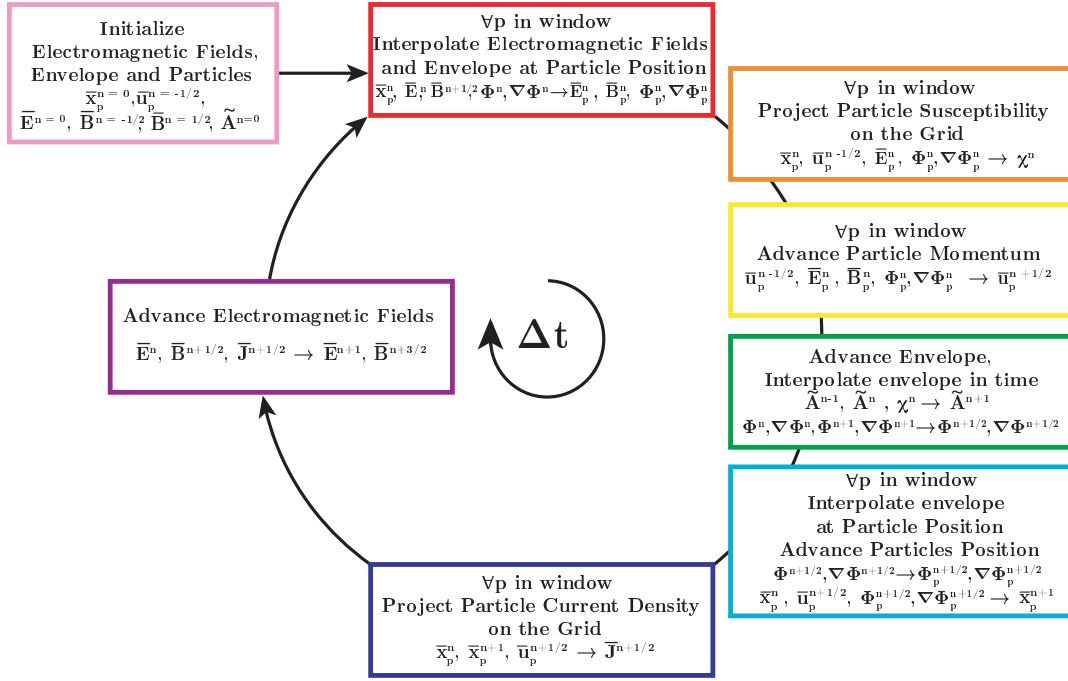


Figure A1: Ponderomotive Particle in Cell loop. The definition of ponderomotive potential  $\Phi = \frac{|\tilde{\mathbf{A}}|^2}{2}$  is used.

MP momentum is known only at the timestep  $n - 1/2$ . Thus, a two step computation (derived in [20]) is used to obtain an approximation of the desired Lorentz factor  $\bar{\gamma}_p^n$ :

$$\gamma_{0p}^2 = 1 + r_s^2 \Phi_p^n + \bar{\mathbf{u}}_p^{n-1/2} \cdot \bar{\mathbf{u}}_p^{n-1/2}, \quad (\text{A.10})$$

$$\bar{\gamma}_p^n = \gamma_{0p} + \frac{1}{2\gamma_{0p}^2} \left( \gamma_{0p} \frac{\Delta t}{2} r_s \bar{\mathbf{E}}^n - \frac{\Delta t}{4} r_s^2 \nabla\Phi_p^n \right) \cdot \bar{\mathbf{u}}_p^{n-1/2}. \quad (\text{A.11})$$

This ponderomotive Lorentz factor  $\bar{\gamma}_p^n$  is used in the deposition of susceptibility, following Eq. A.2.

A modified Boris pusher [6] can be used to update the MP momenta. The only modifications to the standard scheme are the use of  $\left( r_s \bar{\mathbf{E}}_p^n - r_s^2 \frac{\nabla\Phi_p^n}{2\bar{\gamma}_p^n} \right)$  instead of  $r_s \bar{\mathbf{E}}_p^n$  as the source term changing the particle  $p$  energy and the term  $r_s \frac{\bar{\mathbf{B}}_p^n}{\bar{\gamma}_p^n}$  for its momentum rotation under the effect of the magnetic field. The ponderomotive Lorentz factor  $\bar{\gamma}_p^n$  used by the pusher is the one from Eq. A.11.

Again, to update the particle  $p$  position through a leapfrog scheme, the necessary ponderomotive Lorentz factor at timestep  $n + 1/2$  cannot be computed directly from Eq. A.3, since the ponderomotive potential  $\Phi$  and its gradient can be interpolated only at the known MP position at timestep  $n$ . Hence, a two-step approximation of the ponderomotive Lorentz factor  $\bar{\gamma}_p^{n+1/2}$  (derived in [20]) is used:

$$\gamma_{0p}^2 = 1 + \bar{\mathbf{u}}_p^{n+1/2} \cdot \bar{\mathbf{u}}_p^{n+1/2} + r_s^2 \Phi_p^{n+1/2}(\bar{\mathbf{x}}_p^n), \quad (\text{A.12})$$

$$\bar{\gamma}_p^{n+1/2} = \gamma_{0p} + \frac{\Delta t}{4\gamma_{0p}^2} \bar{\mathbf{u}}_p^{n+1/2} \cdot r_s^2 \nabla\Phi_p^{n+1/2}(\bar{\mathbf{x}}_p^n). \quad (\text{A.13})$$

Note that the ponderomotive potential and its gradient in Eqs. A.12, A.13 are defined at the timestep  $n + 1/2$ . Since these quantities known at the timesteps  $n$  and  $n + 1$ , their value at  $n + 1/2$  can be obtained through linear interpolation. After this interpolation in time, they are interpolated at the known particle position at the timestep  $n$  and then used to compute  $\bar{\gamma}_p^{n+1/2}$  through Eqs. A.12, A.13.

Finally, using  $\bar{\gamma}_p^{n+1/2}$  of Eq. A.13, the updated position can be computed:

$$\bar{\mathbf{x}}_p^{n+1} = \bar{\mathbf{x}}_p^n + \frac{\bar{\mathbf{u}}_p^{n+1/2}}{\bar{\gamma}_p^{n+1/2}} \Delta t. \quad (\text{A.14})$$



## Acknowledgments

F. Massimo was supported by P2IO LabEx (ANR-10-LABX-0038) in the framework “Investissements d’Avenir” (ANR-11-IDEX-0003-01) managed by the Agence Nationale de la Recherche (ANR, France). This work was granted access to the HPC resources of TGCC/CINES under the allocation 2018-A0050510062 and Grand Challenge “Irene” 2018 project gch0313 made by GENCI. The authors are grateful to the TGCC and CINES engineers for their support. The authors thank the engineers of the LLR HPC clusters for resources and help. The authors are grateful to the ALaDyn development team for the help and discussions during the development of the envelope model, in particular D. Terzani, A. Marocchino and S. Sinigardi and to Gilles Maynard for fruitful discussions.

## Bibliography

- [1] T. Tajima and J. M. Dawson. Laser electron accelerator. *Phys. Rev. Lett.*, 43:267–270, Jul 1979.
- [2] V. Malka, S. Fritzler, E. Lefebvre, M.-M. Aeonard, F. Burgy, J.-P. Chambaret, J.-F. Chemin, K. Krushelnick, G. Malka, S. P. D. Mangles, Z. Najmudin, M. Pittman, J.-P. Rousseau, J.-N. Scheurer, B. Walton, and A. E. Dangor. Electron acceleration by a wake field forced by an intense ultrashort laser pulse. *Science*, 298(5598):1596–1600, 2002.
- [3] E. Esarey, C. B. Schroeder, and W. P. Leemans. Physics of laser-driven plasma-based electron accelerators. *Rev. Mod. Phys.*, 81:1229–1285, Aug 2009.
- [4] V. Malka. Laser plasma accelerators. *Physics of Plasmas*, 19(5):055501, 2012.
- [5] B. Cros, B.S. Paradkar, X. Davoine, A. Chancé, F.G. Desforges, S. Dobosz-Dufrénoy, N. Delerue, J. Ju, T.L. Audet, G. Maynard, M. Lobet, L. Gremillet, P. Mora, J. Schwindling, O. DelferriÅsre, C. Bruni, C. Rimbault, T. Vinatier, A. Di Piazza, M. Grech, C. Riconda, J.R. MarquÅss, A. Beck, A. Specka, Ph. Martin, P. Monot, D. Normand, F. Mathieu, P. Audebert, and F. Amiranoff. Laser plasma acceleration of electrons with multi-pw laser beams in the frame of cilex. *Nuclear Instruments and Methods in Physics Research Section A: Accelerators, Spectrometers, Detectors and Associated Equipment*, 740:27 – 33, 2014. Proceedings of the first European Advanced Accelerator Concepts Workshop 2013.
- [6] C. K. Birdsall and A. B. Langdon. *Plasma Physics via Computer Simulation*. Taylor and Francis Group, 2004.
- [7] X. Davoine, E. Lefebvre, J. Faure, C. Rechatin, A. Lifschitz, and V. Malka. Simulation of quasimonoenergetic electron beams produced by colliding pulse wakefield acceleration. *Physics of Plasmas*, 15(11):113102, 2008.
- [8] E. Esarey, P. Sprangle, J. Krall, and A. Ting. Self-focusing and guiding of short laser pulses in ionizing gases and plasmas. *IEEE Journal of Quantum Electronics*, 33(11):1879–1914, Nov 1997.
- [9] Patrick Mora and Jr. Thomas M. Antonsen. Kinetic modeling of intense, short laser pulses propagating in tenuous plasmas. *Physics of Plasmas*, 4(1):217–229, 1997.
- [10] A. Lifschitz, X. Davoine, E. Lefebvre, J. Faure, C. Rechatin, and V. Malka. Particle-in-Cell modelling of laser–plasma interaction using Fourier decomposition. *Journal of Computational Physics*, 228(5):1803–1814, November 2008.
- [11] J.-L. Vay. Noninvariance of space- and time-scale ranges under a lorentz transformation and the implications for the study of relativistic interactions. *Phys. Rev. Lett.*, 98:130405, Mar 2007.
- [12] C. Benedetti, C. B. Schroeder, E. Esarey, C. G. R. Geddes, and W. P. Leemans. Efficient modeling of laser-plasma accelerators with inf&rno. *AIP Conference Proceedings*, 1299(1):250–255, 2010.
- [13] Carlo Benedetti, Eric Esarey, Wim P. Leemans, and Carl B. Schroeder. Efficient Modeling of Laser-plasma Accelerators Using the Ponderomotive-based Code INF&RNO. In *Proceedings, 11th International Computational Accelerator Physics Conference (ICAP 2012): Rostock-Warnemünde, Germany, August 19-24, 2012*, page THAA12, 2012.
- [14] F. Massimo, S. Atzeni, and A. Marocchino. Comparisons of time explicit hybrid kinetic-fluid code architect for plasma wakefield acceleration with a full pic code. *Journal of Computational Physics*, 327(Supplement C):841 – 850, 2016.
- [15] D. F. Gordon, W. B. Mori, and T. M. Antonsen. A ponderomotive guiding center particle-in-cell code for efficient modeling of laser-plasma interactions. *IEEE Transactions on Plasma Science*, 28(4):1135–1143, Aug 2000.
- [16] C. Huang, V.K. Decyk, C. Ren, M. Zhou, W. Lu, W.B. Mori, J.H. Cooley, T.M. Antonsen, and T. Katsouleas. Quickpic: A highly efficient particle-in-cell code for modeling wakefield acceleration in plasmas. *Journal of Computational Physics*, 217(2):658 – 679, 2006.
- [17] Benjamin M. Cowan, David L. Bruhwiler, Estelle Cormier-Michel, Eric Esarey, Cameron G.R. Geddes, Peter Messmer, and Kevin M. Paul. Characteristics of an envelope model for laser–plasma accelerator simulation. *Journal of Computational Physics*, 230(1):61 – 86, 2011.
- [18] A. Helm, J. Vieira, L. Silva, and R. Fonseca. Implementation of a 3D version of ponderomotive guiding center solver in particle-in-cell code OSIRIS. In *APS Meeting Abstracts*, page GP10.011, October 2016.
- [19] C Benedetti, C B Schroeder, C G R Geddes, E Esarey, and W P Leemans. An accurate and efficient laser-envelope solver for the modeling of laser-plasma accelerators. *Plasma Physics and Controlled Fusion*, 60(1):014002, 2018.
- [20] Davide Terzani and Pasquale Londrillo. A fast and accurate numerical implementation of the envelope model for laser-plasma dynamics. *Computer Physics Communications*, 242:49 – 59, 2019.
- [21] J. Derouillat, A. Beck, F. Pérez, T. Vinci, M. Chiramello, A. Grassi, M. Flé, G. Bouchard, I. Plotnikov, N. Aunai, J. Dargent, C. Riconda, and M. Grech. Smilei : A collaborative, open-source, multi-purpose particle-in-cell code for plasma simulation. *Computer Physics Communications*, 222:351 – 373, 2018.
- [22] Arnaud Beck, Julien Derouillat, Mathieu Lobet, Asma Farjallah, Francesco Massimo, Imen Zemzemi, Frédéric Perez, Tommaso Vinci, and Mickael Grech. Adaptive SIMD optimizations in particle-in-cell codes with fine-grain particle sorting. *Computer Physics Communication*, (in press) 2019.
- [23] Brice Quesnel and Patrick Mora. Theory and simulation of the interaction of ultraintense laser pulses with electrons in vacuum. *Phys. Rev. E*, 58:3719–3732, Sep 1998.
- [24] G. Z. Sun, E. Ott, Y. C. Lee, and P. Guzdar. Self focusing of short intense pulses in plasmas. *The Physics of Fluids*, 30(2):526–532, 1987.
- [25] K. Yee. Numerical solution of initial boundary value problems involving maxwell’s equations in isotropic media. *IEEE Transactions on Antennas and Propagation*, 14:302–307, May 1966.



- 1  
2 [26] T.Zh. Esirkepov. Exact charge conservation scheme for particle-in-cell simulation with an arbitrary form-factor. *Computer Physics Communications*, 135(2):144 – 153, 2001.
- 3 [27] R. J. Shalloo, C. Arran, A. Picksley, A. von Boetticher, L. Corner, J. Holloway, G. Hine, J. Jonnerby, H. M. Milchberg, C. Thornton, R. Walczak, and S. M. Hooker. Low-density hydrodynamic optical-field-ionized plasma channels generated with an axicon lens. *Phys. Rev. Accel. Beams*, 22:041302, Apr 2019.
- 4 [28] Xiangkun Li, Alban Mosnier, and Phu Anh Phi Nghiem. Design of a 5 gev laser-plasma accelerating module in the quasi-linear regime. *Nuclear Instruments and Methods in Physics Research Section A: Accelerators, Spectrometers, Detectors and Associated Equipment*, 2018.
- 5 [29] R. Lehe, A. Lifschitz, C. Thauray, V. Malka, and X. Davoine. Numerical growth of emittance in simulations of laser-wakefield acceleration. *Phys. Rev. ST Accel. Beams*, 16(2):021301, 2013.
- 6 [30] J.-L. Vay, C.G.R. Geddes, E. Cormier-Michel, and D.P. Grote. Numerical methods for instability mitigation in the modeling of laser wakefield accelerators in a lorentz-boosted frame. *Journal of Computational Physics*, 230(15):5908 – 5929, 2011.
- 7 [31] J.-L. Vay. Simulation of beams or plasmas crossing at relativistic velocity. *Physics of Plasmas*, 15(5):056701, 2008.
- 8 [32] F. Massimo, A. Marocchino, and A.R. Rossi. Electromagnetic self-consistent field initialization and fluid advance techniques for hybrid-kinetic pwfa code architect. *Nuclear Instruments and Methods in Physics Research Section A: Accelerators, Spectrometers, Detectors and Associated Equipment*, 829(Supplement C):378 – 382, 2016. 2nd European Advanced Accelerator Concepts Workshop - EAAC 2015.
- 9 [33] Sailing He and Vaughan H. Weston. Wave-splitting and absorbing boundary condition for maxwell’s equations on a curved surface. *Mathematics and Computers in Simulation*, 50(5):435 – 455, 1999.
- 10 [34] Hélène Barucq and Bernard Hanouzet. Asymptotic behavior of solutions to maxwell’s system in bounded domains with absorbing silver–mueller’s condition on the exterior boundary. *Asymptotic Analysis*, 15:25 – 40, 1997.
- 11 [35] Jean-Luc Vay. A new absorbing layer boundary condition for the wave equation. *Journal of Computational Physics*, 165(2):511 – 521, 2000.
- 12 [36] M. Karkkainen, E. Gjonaj, T. Lau, and T. Weiland. Low-dispersion wake field calculation tools. *Proceedings of ICAP*, (1):35.
- 13 [37] Benjamin M. Cowan, David L. Bruhwiler, John R. Cary, Estelle Cormier-Michel, and Cameron G. R. Geddes. Generalized algorithm for control of numerical dispersion in explicit time-domain electromagnetic simulations. *Phys. Rev. ST Accel. Beams*, 16:041303, Apr 2013.
- 14 [38] S. Jalas, I. Dornmair, R. Lehe, H. Vincenti, J.-L. Vay, M. Kirchen, and A. R. Maier. Accurate modeling of plasma acceleration with arbitrary order pseudo-spectral particle-in-cell methods. *Physics of Plasmas*, 24(3):033115, 2017.
- 15 [39] Remi Lehe, Manuel Kirchen, Brendan B. Godfrey, Andreas R. Maier, and Jean-Luc Vay. Elimination of numerical cherenkov instability in flowing-plasma particle-in-cell simulations by using galilean coordinates. *Phys. Rev. E*, 94:053305, Nov 2016.
- 16 [40] M. Kirchen, R. Lehe, B. B. Godfrey, I. Dornmair, S. Jalas, K. Peters, J.-L. Vay, and A. R. Maier. Stable discrete representation of relativistically drifting plasmas. *Physics of Plasmas*, 23(10):100704, 2016.
- 17 [41] A. Beck, S.Y. Kalmykov, X. Davoine, A. Lifschitz, B.A. Shadwick, V. Malka, and A. Specka. Physical processes at work in sub-30fs, pw laser pulse-driven plasma accelerators: Towards gev electron acceleration experiments at cilex facility. *Nuclear Instruments and Methods in Physics Research Section A: Accelerators, Spectrometers, Detectors and Associated Equipment*, 740:67 – 73, 2014. Proceedings of the first European Advanced Accelerator Concepts Workshop 2013.
- 18 [42] Chandrasekhar Roychoudhuri. Fundamentals of photonics. 2008.
- 19 [43] W. Lu, M. Tzoufras, C. Joshi, F. S. Tsung, W. B. Mori, J. Vieira, R. A. Fonseca, and L. O. Silva. Generating multi-gev electron bunches using single stage laser wakefield acceleration in a 3d nonlinear regime. *Phys. Rev. ST Accel. Beams*, 10:061301, Jun 2007.
- 20 [44] M. Tzoufras, W. Lu, F. S. Tsung, C. Huang, W. B. Mori, Thomas C. Katsouleas, J. Vieira, R. A. Fonseca, and L. O. Silva. Beam loading in the nonlinear regime of plasma-based acceleration. *Phys. Rev. Lett.*, 101:145002, 2008.
- 21  
22  
23  
24  
25  
26  
27  
28  
29  
30  
31  
32  
33  
34  
35  
36  
37  
38  
39  
40  
41  
42  
43  
44  
45  
46  
47  
48  
49  
50  
51  
52  
53  
54  
55  
56  
57  
58  
59  
60